Numerical and Experimental Study of Wing Tip Endplates of a Formula Student Car

Tiago Pereira Rocha
tiago.pereira.rocha@tecnicno.ulisboa.pt

Instituto Superior Técnico, Universidade de Lisboa, Portugal

October 2020

Abstract

The aerodynamic appendages of Formula Student cars, are getting more intricate as time goes by, as the gains are getting more and more marginal. Given the low speeds achieved by Formula Student cars and the geometric restrictions imposed by the rules, the downforce generated on the cars will imply very high drag forces. It is this project's aim to propose a different design for the endplate of the rear wing of such a car. By making use of airfoils, effectively converting the endplate from a flat plate into a vertical wing, the characteristics of the rear wing assembly are changed – reducing the induced angle of attack, decreasing the drag coefficient without loss of lift coefficient, thereby increasing its efficiency. First, a mesh convergence analysis was performed to assess the numerical accuracy of the simulations. Then, simulations were done with a single element wing in order to assess the hypothesis, as well as to understand how geometric factors contributed to the performance of the wing. The concept was afterwards applied to the full wing. Finally, a 40%-scale model of the simulated wing was constructed with 3D printing in order to test it in the wind tunnel: first at the low Reynolds tunnel of the Fluids Laboratory; and at a later time at the CCTAE tunnel. The results were compared with the CFD simulations, confirming the potential of the concept theorized at the inception of the project.
Keywords: Formula Student, finite wings, endplates, CFD, wind tunnel

1. Introduction

The aerodynamics of racecars has been an important performance differentiator since the end of 1960s, when wings were first used in F1 [1]. The aerodynamic devices increase the normal load on the tyres, decreasing the tyre slip, β, needed to generate the same horizontal force [1].

$$\mu = \frac{F_\xi}{F_Z} \tag{1}$$

where F_ξ is a force component parallel to the ground and F_Z is the normal force component. The downforce generated does not add weight to the car, enlarging the tyre's performance envelope.

The main contributors to the downforce of a race car are usually its wings and undertray, while the drag is mostly caused by the rear wing and wheels [2].

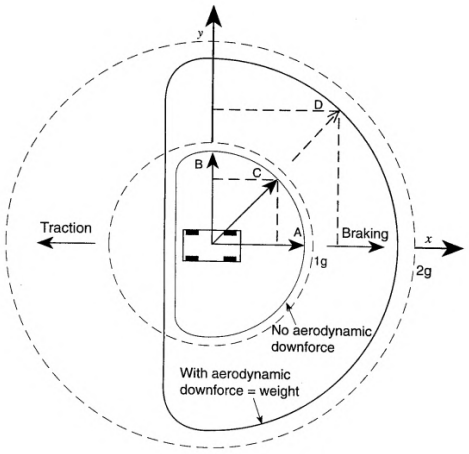

Figure 1: Schematic of the tyre's performance envelope. The downforce enlarges the range of operation of the tyre [1].

1.1. Aerodynamics in Formula Student

Formula Student is a worldwide competition for university students in which they conceive, fabricate and compete with prototypes in several static and dynamic events [3]. Points are awarded for each event, with an emphasis in the car's on-track performance.

Nowadays, the aerodynamic appendages of Formula Student cars play a big role in their performance, and have been getting more complex year-

on-year (Figure 2). The wings are responsible for almost 75% of the downforce, and the single highest contributor for the total drag is the rear wing (Table 1).

Figure 2: Ecurie Aix, from the RWTH Aachen, participating at FSG 2019 with its eace08 car. See the complex aerodynamic package.

Due to regulatory constraints, the rear wing of Formula Student cars have a very low aspect ratio, resulting in the aforementioned significant drag contribution to the overal drag of the car. In trying to further increase the downforce of the cars, gurney flaps are usually added to the trailing edge of the rear wings' endplates (Figure 3). This generates separation, leading to a drag penalty.

Figure 3: Gurney flap on an endplate of a FS car.

This project proposes an alternative to the gurney flap by using airfoils as the section of the wing endplates. This turns the endplates into lifting surfaces, which will reduce the induced angle of attack α_i, thereby reducing the induced drag D_i, increasing the wing's and car's aerodynamic efficiency.

The altenative solution was first studied with CFD simulations in Star-CCM+. Different airfoils were tested, as well as varying endplate sizes. Afterwards a scale model was constructed and tested in the wind tunnel to confirm the trends observed in the simulations.

2. Mathematical Models

2.1. Airflow Characterisation

The Reynolds number is defined as the ratio between inertial and diffusion forces of the fluid.

$$Re = \frac{\rho V L}{\mu} = \frac{V L}{\nu} \tag{2}$$

where V is the free-stream velocity (m/s), L is the reference length of the flow (m), μ is the dynamic viscosity $(kg/(m \cdot K))$, and ν is the kinematic viscosity, defined by $\nu = \mu/\rho$ $(m^{-2}K^{-1})$.

The Re of this case is calculated considering $U = 15m/s$, corresponding to the average velocity over a lap at a FS track, L is the total chord of the rear wing of FST09e, $L = 0.4 + 0.2 + 0.2 = 0.8m$, and ρ and μ are the density and dynamic viscosity of the air, respectively $1.225kg/m^3$ and $1.81 \times 10^{-5} kg/(m \cdot s)$ at $15° C$. These values yield a $Re \approx 8 \times 10^5$.

At this Reynolds number, transition may be present on the wing and play a role on the development of the boundary-layers on the wings' surfaces.

2.2. RANS Equations and Turbulence Models

In the simulations, the flow was assumed to have constant properties and to be statiscally steady. Therefore, the RANS (Reynolds-Averaged Navier Stokes) were used (Equations 3 and 4).

$$\rho \frac{\partial \bar{u}_i}{\partial x_i} = 0 \tag{3}$$

$$\rho \bar{u}_j \frac{\partial \bar{u}_i}{\partial x_j} = \rho \bar{f}_i + \frac{\partial}{\partial x_j} \left[-\bar{p}\delta_{ij} + \mu \left(\frac{\partial \bar{u}_i}{\partial x_j} + \frac{\partial \bar{u}_j}{\partial x_i} \right) - \rho \overline{u_i' u_j'} \right] \tag{4}$$

This set of equations needs to be closed with a turbulence model. In this case, given the expected adverse pressure gradients and separation areas, the SST k-w model was used [4] (Equations 5 and 6. It combines the k-e and k-w models, profiting from the robustness of the k-w model near the wall and the free-stream independence of the k-e model, and also features an eddy viscosity limiter.(Equation 7)

$$\begin{aligned} \frac{\partial(\rho k)}{\partial t} + \frac{\partial(\rho u_j k)}{\partial x_j} &= P - \beta^* \rho \omega k \\ &+ \frac{\partial}{\partial x_j} \left[(\mu + \sigma_k \mu_t) \frac{\partial k}{\partial x_j} \right] \end{aligned} \tag{5}$$

$$\begin{aligned} \frac{\partial(\rho \omega)}{\partial t} + \frac{\partial(\rho u_j \omega)}{\partial x_j} &= \frac{\gamma}{\nu_t} P - \beta \rho \omega^2 \\ + \frac{\partial}{\partial x_j} \left[(\mu + \sigma_\omega \mu_t) \frac{\partial \omega}{\partial x_j} \right] &+ 2(1 - F_1) \frac{\rho \sigma_{\omega 2}}{\omega} \frac{\partial k}{\partial x_j} \frac{\partial \omega}{\partial x_j} \end{aligned} \tag{6}$$

Component	Drag Coefficient		Lift Coefficient		C_L/C_D
	C_D	Proportion [%]	C_L	Proportion [%]	
Front Wing	-0,175	13,7	-1,165	39,8	6,669
Rear Wing	-0,487	38,1	-1,010	34,5	2,072
Undertray	-0,140	10,9	-0,697	23,8	4,994
Front Wheels	-0,066	5,1	0,051	-1,7	-0,780
Rear Wheels	-0,074	5,8	0,037	-1,2	-0,495
Sidepod	0,013	-1,0	0,105	-3,6	8,154
Rest	-0,350	27,4	-0,247	8,4	0,706
Total	-1,278	100	-2,926	100	2,289

Table 1: C_D and C_L distribution over different parts on a FS car. Values provided by FST Lisboa.

$$\mu_t = \frac{\rho a_1 k}{\max(a_1\omega, \Omega F_2)} \tag{7}$$

The model constants are obtained from $C = F_1C_1 + (1 - F_1)C_2$, where the constants C_1 pertain to the SST k-w model, while the C_2 constants are taken from the standard k-e model.

$$\sigma_{k1} = 0.85, \sigma_{w1} = 0.5, \beta_1 = 0.0750, a_1 = 0.31$$
$$\beta^* = 0.09, k = 0.41, \gamma_1 = \beta_1/\beta^* - \sigma_{w1}k^2/\sqrt{\beta^*} \tag{8}$$

$$\sigma_{k2} = 1.0, \sigma_{w2} = 0.856, \beta_2 = 0.0828$$
$$\beta^* = 0.09, k = 0.41, \gamma_2 = \beta_2/\beta^* - \sigma_{w2}k^2/\sqrt{\beta^*} \tag{9}$$

2.3. Transition Model

The GammaReTheta Transition Model (γRe_θ) [5] was also used to assess the transition from laminar to turbulent flow, as well as the existence of laminar separation bubbles on the airfoil. The model solves for intermittency, γ, and transition momentum thickness Reynolds number, $\overline{Re_{\theta t}}$ (Equations 11 and 13).

$$\frac{\partial(\rho\gamma)}{\partial t} + \frac{\partial(\rho U_j\gamma)}{\partial x_j} = \tag{10}$$
$$P_\gamma - E_\gamma + \frac{\partial}{\partial x_j}\left[\left(\mu + \frac{\mu_t}{\sigma_f}\right)\frac{\partial\gamma}{\partial x_j}\right] \tag{11}$$

$$\frac{\partial(\rho\overline{Re_{\theta t}})}{\partial t} + \frac{\partial(\rho U_j\overline{Re_{\theta t}})}{\partial x_j} = \tag{12}$$
$$P_{\theta t} + \frac{\partial}{\partial x_j}\left[\sigma_{\theta t}(\mu + \mu_t)\frac{\partial\overline{Re_{\theta t}}}{\partial x_j}\right] \tag{13}$$

3. Mesh Convergence Analysis

3.1. Pre-processing - Geometry and Mesh

A mesh convergence analysis was done to assess the numerical error of the simulations. The model used was that of the rear wing of FST Lisboa's FST09e car (Figure 4). The domain was large enough so that the boundaries would not interfere with the flow around the wing (Figure 5).

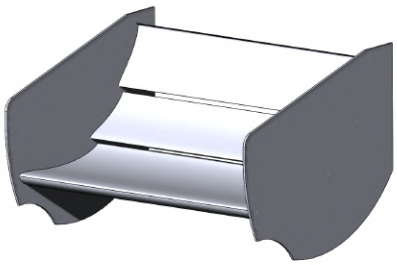

Figure 4: Geometry used for the mesh convergence analysis.

Figure 5: Domain used in the CFD simulations.

A trimmed (hexahedral) mesh was used. Prism layers were added to all the wing's surfaces, so that the flow near them could be better resolved and comply with the requirement $y^+ = 1$. Figure 6

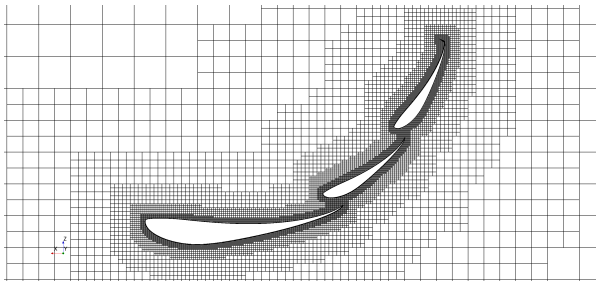

Figure 6: Mesh on symmetry plane.

shows the mesh on the symmetry plane of the wing.

The boundary conditions are shown in Figure 7. The inlet is defined as a velocity-inlet with velocity magnitude $V = 15m/s$; the outlet is a pressure outlet, with the pressure being set to $0Pa$ (Gauge); the ground is a no-slip wall that moves at the same velocity as the airflow, $V_{ground} = V$; the top and side boundaries, because they are far away from the wing, are defined as symmetry planes; the symmetry boundary is a symmetry plane; the wing's surfaces are defined as stationary ($V_{wing} = 0m/s$) no-slip walls.

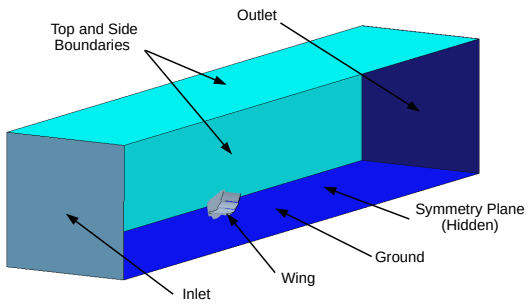

Figure 7: Boundary conditions.

3.2. Results

Five different meshes were used for the mesh convergence analysis, whose results are in Table 2. Using the Richardson extrapolation [6], the exact solution was estimated as well as its error constant. These values are presented in Table 3

The data obtained with the mesh convergence analysis had some noise due to the definition of r, since it is difficult ensure the same r in each refinement step of an unstructured trimmed (hexahedral) mesh. Nonetheless, the estimated numerical errors are close to or smaller than 1%. Based on these results, the mesh used for the next simulations was the fine mesh.

3.3. Transition Model

The SST k-w model usually predicts transition at around $Re = 5 \times 10^4$ [7], below the natural transition Reynolds number. Therefore the $\gamma - Re_\theta$transition model was tested on the same mesh as the k-w model to see if there were differences in the airflow.

There was a noticeable difference in the point at which transition occurs, seen in the skin friction coefficient plots along the x-coordinate (Figures 9 and 8). In the case of the SST k-w model, there is a peak at $x \approx 1.35$, right after the leading-edge of the main element of the wing. This means that at that point the transition from laminar to turbulent flow had already occured, which corresponds to $x_{crit} = 0.025c_t$. The $\gamma - Re_\theta$model revealed a different location for the transition, at $x_{crit} \approx 0.15c_t$. Besides, the transition occurs with a laminar separation bubble. This can be seen in the C_f plot of 9 where $C_f = 0$ at the x_{crit}.

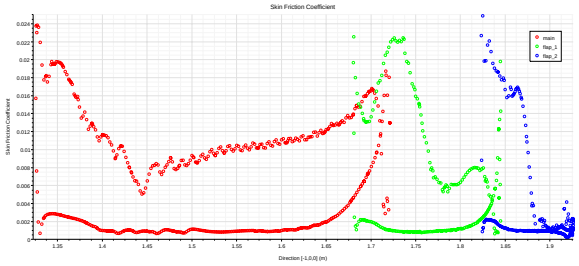

Figure 8: C_f plot of the SST-kw model at $y = 0.5b$.

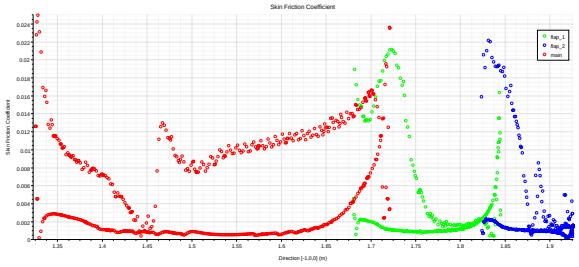

Figure 9: C_f plot of the k-w at $y = 0.5b$.

The values of the coefficients with the two models are given in Table 4. The difference for both is within the error estimation of the previous section. However, given that the physics of the flow is different, the $\gamma - Re_\theta$model had to be chosen for the remainder of the projects' simulations.

Mesh	Mesh Parameters					Results	
	TSS [mm]	NPL	PLIH [mm]	NE ($\times 10^6$)	r	C_L	C_D
Coarse	4	7	0.0462	1.5	—	2.617	1.068
Medium-Coarse	3.5	8	0.0362	2.1	1.12	2.637	1.083
Medium	3	10	0.0230	3.2	1.27	2.626	1.073
Medium-Fine	2.3	13	0.0123	5.9	1.57	2.627	1.078
Fine	2	15	0.0083	8.7	1.78	2.600	1.064

Table 2: Data retrieved from the mesh convergence analysis. TSS is the target surface size; NPL is the number of prism layers; PLIH is the prism layer initial height; NE is the number of elements in the mesh; and r is the refinement factor, $r = \sqrt[3]{h_i/h_1}$.

	C_L	C_D
ϕ_0	2.540	1.051
ϕ	6.034E-02	1.217E-02

Table 3: Guess of the exact solution and error constant of the mesh convergence analysis. ϕ_0 is the estimate of the exact solution, and ϕ is the error.

4. Results

4.1. CFD Simulations

Geometry Model The geometry used for the the simulations was a wing with only the main plane with the same characteristics of the full wing used in the mesh convergence analysis. An emphasis was put into understanding how the location of the top and bottom extremities of the endplate had on the performance of the wing.

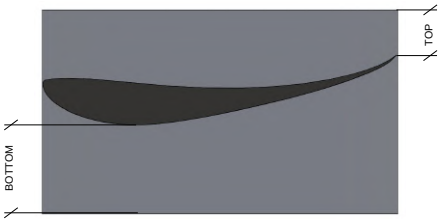

Figure 10: Variable dimensions of the endplate analyses.

4.1.1 First Tests

The first simulations were done with two geometries. A flat endplate (the usual design) and an endplate with the NACA2412 airfoil. In them, the endplate had the following dimensions: $top = 0mm \vee bottom = 50mm$ and $top = bottom = 50mm$. In the case of $top = 0mm \vee bottom = 50mm$, the C_L was larger and the C_D smaller for the flat endplate, resulting in a higher C_L/C_D than that of the 2412 endplate . With $top = bottom = 50mm$, the C_L of the flat endplate was still larger, but the C_D was higher too. The consequence is that the 2412 endplate now has an efficiency only 1.65% smaller than that of the flat endplate. Despite the increase in C_L/C_D and lower C_D , the C_L of the 2412 endplate falls short of that flat endplate by -8.3%. A factor could have been the decrease in span of the main element due to the airfoil thickness, since the span of wing overall has to stay the same due to the rules. A thinner 2402 airfoil was then simulated for the same endplate dimensions, which compared favorably against the flat endplate: higher C_L , identical C_D and a higher C_L/C_D . When increasing the top dimension, though, both the C_L and C_D are smaller than those of the flat endplate, with the C_L/C_D still larger owing to a bigger decrease in the C_D .

Therefore, a new set of simulations was done with different endplate dimensions for the flat and 2402 endplates. The force coefficients of these simulations for $top = 50mm$ and varying $bottom$ are in Table 5, and the drag components of the $top = 50mm$ and $bottom = 200mm$ are in Tables 6.

Increasing the bottom dimension leads to identical C_D values of the 2402 endplate when compared with the flat one, but the increase in C_L is more noticeable, with the gains in term of C_L/C_D evident, reaching a maximum increase of 10.4% for the $top = 50mm \vee bottom = 200mm$. Looking at the different drag components, the introduction of the airfoil to the endplate reduces the wing's overall drag by reducing the endplate's pressure and viscous drag. The viscous and pressure drag values of the main wing increase somewhat with the 2402 endplate, however, resulting in a larger main wing total drag. Still, this increase is not enough to offset the drag reduction of the endplate.

Model	C_L	$\Delta\%$	C_D	$\Delta\%$	C_L/C_D	$\Delta\%$
SST K-w	2.600		1.064		2.445	
$\gamma - Re_\theta$	2.660	+2.308	1.097	+3.101	2.425	-0.818

Table 4: Comparison between the SST k-w and $\gamma - Re_\theta$models.

Endplate	Bottom [mm]	Lift [N]	Drag [N]	C_L	C_D	C_L /C_D
Flat	100	26.295	3.466	1.115	0.147	7.587
	150	27.177	3.512	1.152	0.149	7.738
	200	27.826	3.548	1.180	0.150	7.843
2402	100	27.072	3.420	1.148	0.145	7.916
	150	28.115	3.389	1.192	0.144	8.296
	200	28.981	3.348	1.229	0.142	8.656

Table 5: Results of the fixed dimension $top = 50mm$.

4.1.2 Four Endplate Designs

Two additional designs were simulated: one the gurney flap, the solution usually used by Formula Student teams; and the NACA2402 with negative camber, to seek maximum efficiency according to the hypothesis tested beforehand. These are shown side-by-side in Figure 11.

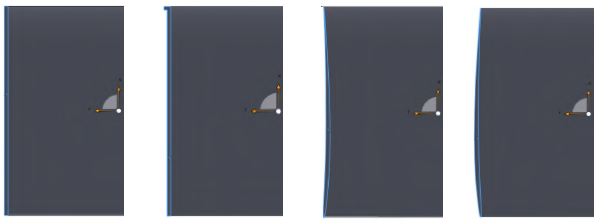

(a) Flat endplate. (b) Gurney flap. (c) NACA2402. (d) NACA2402inv

Figure 11: Final endplate designs for comparison.

The endplate with the 2402 airfoil has the highest C_L (Figure 12) values followed by the endplate with the gurney flap, the flat endplate and then the inverted 2402 airfoil. The fact that the gurney flap increases the C_L so much and close to the 2402 airfoil corroborates the theory that its effect is similar to that of the airfoil in terms of giving a camber to the endplate. Regarding the C_D values, plotted in Figure 13, the lowest value corresponds to the 2402inv, then the 2402 endplate, the flat endplate and finally the gurney flap by a big margin. The largest C_D value of the gurney flap is a consequence of how the lift increase is obtained, namely due to a separation on its rearward face. Interestingly the trends of the values are opposite: the C_D of the flat plate seems to stabilize with increasing bottom coordinate, while the 2402 is decreasing and the 2402inv increasing. The efficiency of the four endplates is n Figure 14. Here, despite the high lift coefficient, the gurney flap has the lowest efficient due to its high C_D coefficient and the flat endplate is consistently the third most efficient wing. Regarding the two airfoil designs, in the first two bottom coordinates the inverted comes ahead, but is then overtaken by the normal 2402 airfoil. The large efficiency values of the 2402inv endplate are by virtue of the marked reduction in its lift coefficient.

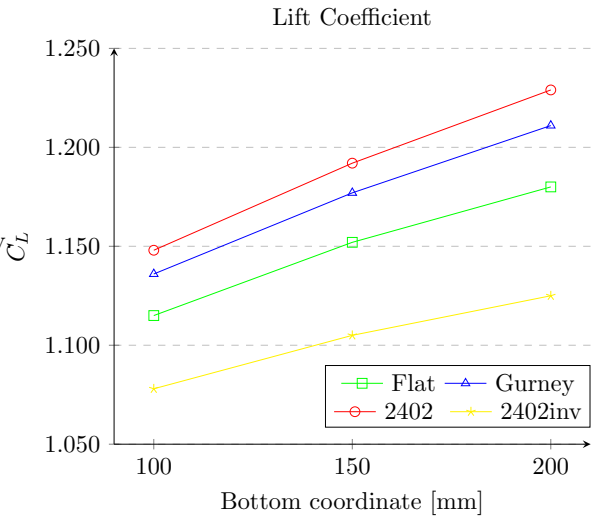

Figure 12: Lift coefficient of the four designs.

4.1.3 Full Wing

The same philosophy was transposed to the full wing. Three geometries were tested: a rectangular flat endplate, a rectangular 2402 endplate, and a 2402 endplate with a cut on the pressure side, mirroring the constant top distance of the best con-

Geometry	Part	Drag Component			C_D Components		
		$D_{pressure}$ [N]	$D_{viscous}$ [N]	D_{total} [N]	$C_{D_{pressure}}$	$C_{D_{viscous}}$	$C_{D_{total}}$
Flat	Endplate	0.398	0.133	0.531	0.017	0.006	0.023
	Main	2.906	0.112	3.017	0.123	0.005	0.128
	Total	3.304	0.245	3.548	0.140	0.010	0.150
2402	Endplate	0.076	0.104	0.180	0.003	0.004	0.008
	Main	3.054	0.114	3.168	0.129	0.005	0.134
	Total	3.130	0.218	3.348	0.133	0.009	0.142

Table 6: Drag components of the Flat and 2402 endplates with $top = 50mm$ and $bottom = 200mm$.

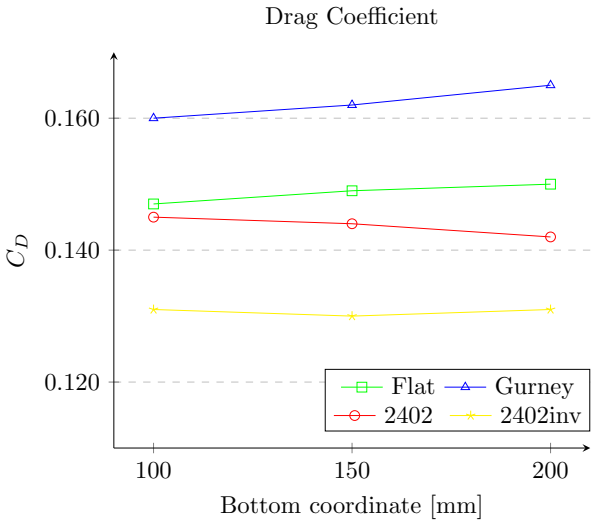

Figure 13: Drag coefficient of the four designs.

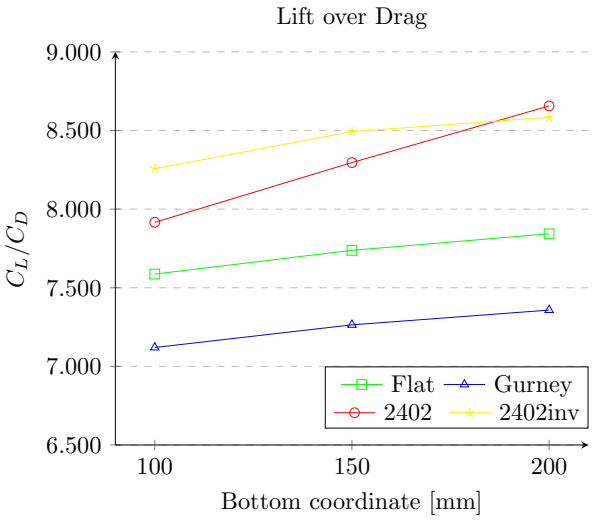

Figure 14: Lift over drag ratio of the four designs.

figuration found with a single wing element. The results are given in table 7.

When the flaps are added, the difference of the curvature introduced in the endplate decreases. In this case, the endplate with the NACA2402 airfoil yields 2% gain in terms of C_L , but a 3.4% increase in C_D , decreasing the overall efficiency of the wing by 1.3%, in contrast with what was seen previously. The design with the cut on the pressure side has -0.8% C_L and more 4% C_D , giving a 4.6% decrease in the C_L /C_D ratio.

The added flaps increase the upwash of the wing, leadint to the airflow leaving the wing at an angle compared with the free-stream. This means that we have effectively two wings working on different planes whose vortexes, due to their different cores' orientations, won't counteract each other in the same way that we saw with the single element wing.

4.2. Experimental Tests

Experimental tests were conducted to confirm the trends observed in the CFD simulations, first at the Fluids Laboratory, and then in the Aeroacoustic wind tunnel of the Aerospace Laboratory. To that effect, a 40%-scale model of the simple wing was constructed with 3D printing. This is shown assembled on the balance of the Fluids Laboratory wind tunnel in figure 15.

4.2.1 Experimental Procedure

Three different geometric configurations were tested: a reference setup without any endplates; the flat endplates; and the endplates with curvature. Data was collected for two different airflow velocities: 7.5 and 15 m/s. For each setup, twenty data acquisitions were performed, each during 20s at the DAQ 150Hz acquisition frequency.

Woolen threads were added to the surfaces of the wing so that the airflow behaviour over the wing could be visualized and compared with the CFD simulations. For the latter experiments sand-paper strips were glued to the model's surfaces. These act as a trip strip, fixing the location of transition from laminar to turbulent flow [8]. This is done in an attempt to emulate the working condition Reynolds flow and minimize the scale effects. A consequence of their use will be the elimination of any separation bubbles [9].

Endplate	Lift [N]	Drag [N]	C_L	C_D	C_L /C_D
Flat	125.505	45.717	2.647	0.964	2.745
NACA2402	128.035	47.275	2.701	0.997	2.708
NACA2402cut	124.504	47.570	2.626	1.003	2.617

Table 7: Results of the full wing designs.

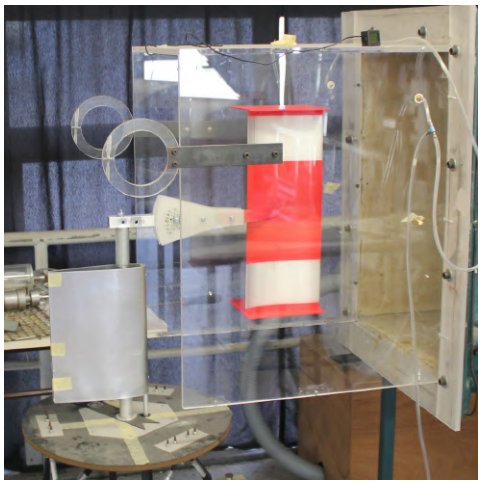

Figure 15: Wing model mounted on the balance at the Fluids Laboratory.

4.2.2 Experimental Tests' Results

Clean Wing The first run was performed for the three configurations described above at two airflow velocities, $\approx 7.5m/s$ and $\approx 15m/s$. The wing was clean, in that there were no woolen threads or sand paper strips. The results are presented in .

For the lower Re, the differences are significant. The 2402 endplate has less lift (11.1%), more drag (35.2) for a smaller efficiency C_L/C_D (34.3%). When the Re was increased, the C_L increased for the two endplates and the C_D decreased, resulting in higher C_L/C_D ratios. The differences between the two endplates at the higher Re were much smaller for each of the three coefficients: 4.5% smaller C_L , a 8.9% increase in C_D and an efficiency 12.3% below the flat endplate. This second set of values points to a significant influence of small Reynolds numbers effects at the lowest flow speed tested.

Sand Paper The sand paper has a considerable influence on the results, which are shown in table 9. With it, for each of the Reynolds numbers tested, the difference between the two endplates is smaller, particularly for the lower Reynolds flow, where the differences for the three coefficients C_L , C_D and C_L/C_D are now, respectively 4.2% (<11.1%), 18.4% (<35.2%) and 19.1% (<34.3%) At $Re = 1.63E + 05$, the C_L is smaller by 5.7%, but the C_D of the 2402 endplate is atually 0.9% smaller than that of the flat endplate, the first occurrence of a value in agreement with the results of the CFD simulations. Combined, the 2402 endplate has an efficiency 4.9% off the flat endplate. This is further evidence that the low Reynolds number flows are not identical to the simulated conditions.

Yaw angles Two yaw-angles (β) were tested for the the two principal configurations – flat plates and 2402 endplates –, whose purpose is to simulate the wing behavior in a cornering condition. The angles chosen were 4 and 8 degrees, based on documentation from FST Lisboa. These two values cover the entire range of angles in a cornering situation at a Formula Student Event. The forces and coefficients are in table 10.

Once again there is a significant difference between the two Reynolds numbers tested. The 2402 endplate has generally again smaller C_L and higher C_D values than the flat one. There are also noteworthy differences across the 3 angles tested. While the difference of the C_L values remain relatively constant for the three angles at each Reynolds number, that is not the case with the C_D values. For $Re = 8.70E + 04$ and $\beta = 4°$, the 2402 endplate only has 5.5% more drag than the flat endplate (the smallest difference of the three C_D coefficients), whereas for $Re = 1.63E + 05$ and $\beta = 4°$ the C_D of the 2402 exhibits the largest difference to the flat endplate at 8.1%. These differences in the C_D values reflect themselves on the efficiency of each of the combinations of endplate and angle, but all below those of the flat endplates. These varying differences hint at a larger importance of the lower Reynolds number at which these tests were conducted.

4.3. CAST Wind Tunnel

At a later time the wing model was also tested at the Aeroacoustic Wind Tunnel of the CAST. The wing mounted on its balance is shown in figure 16. Four different airflow velocities were tested for each of the three geometric configurations, from 15m/s up to 37.5m/s. The maximum airflow speed allowed for flow similarity with the simulations. The results

Analysis	Velocity [m/s]	Re	Lift [N]	Drag [N]	C_L	C_D	C_L/C_D
No-Endplates	7.823	8.50E+04	0.44521	0.04215	0.186	0.018	10.563
	14.781	1.61E+05	1.64069	0.11867	0.192	0.014	13.825
Flat Plate	7.851	8.53E+04	0.58894	0.04049	0.244	0.017	14.545
	14.800	1.61E+05	2.22239	0.12462	0.259	0.015	17.833
NACA2402	7.872	8.56E+04	0.52618	0.05504	0.217	0.023	9.559
	14.833	1.61E+05	2.13202	0.13637	0.247	0.016	15.635

Table 8: Data for the first experiment with the clean wing.

Analysis	Velocity [m/s]	Re	Lift [N]	Drag [N]	C_L	C_D	C_L/C_D
Flat Plate	8.040	8.74E+04	0.47473	0.05209	0.187	0.021	9.114
	14.948	1.63E+05	1.85127	0.14411	0.211	0.016	12.846
NACA2402	8.001	8.70E+04	0.45046	0.06109	0.180	0.024	7.374
	14.989	1.63E+05	1.75520	0.14362	0.199	0.016	12.221

Table 9: Sand paper on all the models' surfaces.

obtain are in table 11.

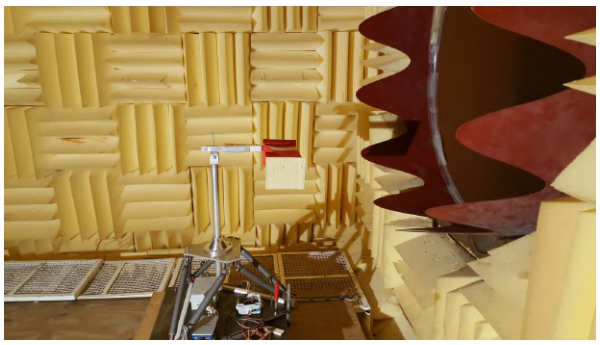

Figure 16: Wing model assembled in the Aeroacoustic Wind Tunnel.

For the lowest Reynolds number, which coincides with the highest Reynolds number tested at the Fluids Laboratory, the trend is the same: the flat endplate has a larger C_L , smaller C_D and a higher C_L/C_D ratio. Regarding the C_L , at the second lowest Re the flat endplate still outperforms the 2402 endplate, but this trend is inverted for the two highest Reynolds numbers. Concerning the C_D this happens from the second lowest Re. This further emphasizes the influence that the low Reynolds number has over the behaviour of the airflow. The efficiency values are a direct consequence of the evolution of the C_L and C_D coefficients, as such is smaller for the 2402 endplate than the flat endplate at the lowest Re, but for the three following Reynolds numbers is concurrent with the CFD simulations. At the highest Reynolds number, which enables the flow similarity, the trend is the same as the one observed with the simulations, indicating that the flow tested is in fact similar to the conditions simulated in CFD. This indicates that the proposed solution is valid for the Reynolds numbers that Formula Student experience.

5. Conclusions

With the CFD simulations, a maximum increase of efficiency of the 2402 endplate of 10.4% when compared against a flat endplate with the same area was achieved. This increase was a result of the double effect of a larger lift coefficient and a smaller drag coefficient. The use of the same concept on a wing with multiple flaps, however, did not yield the same results, which is something that should be further looked into.

The wind tunnel testing provided two sets of data. The experiments in the fluids laboratory showed a significant effect of the Reynolds number on the force coefficients. It also showed that, even though it is a low Reynolds wind tunnel, where the Reynolds and scale effects are large, meaningful results and conclusions can be drawn from it. This is especially true when combined with the extra simulations mimicking the wind tunnel conditions since they exhibited similar trends. The tests done at the CAST were the final proof of validity of the concept that was developed in the simulations. It was possible to explore scale effects and confirm the trends obtained in the simulations and the strong effect of the Reynolds number. Unfortunately, it was not possible to perform the tests with a yaw angle in the CAST.

Acknowledgements

I would like to thank my supervisor, professor Luís Eça, not only for the guidance and feedback; the Formula Student Técnico team, in particular to Inês Viveiros, Luís Morais and Jaime Pacheco, for the availability and assistance whenever needed; pro-

Analysis	β [º]	Velocity [m/s]	Re	Lift [N]	Drag [N]	C_L	C_D	C_L/C_D
Flat Plate	0	8.040	8.74E+04	0.47473	0.05209	0.187	0.021	9.114
		14.948	1.63E+05	1.85127	0.14411	0.211	0.016	12.846
	4	7.726	8.40E+04	0.46504	0.05801	0.199	0.025	8.017
		15.127	1.64E+05	1.83727	0.14996	0.205	0.017	12.252
	8	7.927	8.62E+04	0.47483	0.05837	0.193	0.024	8.135
		14.765	1.61E+05	1.69659	0.17045	0.199	0.020	9.953
NACA2402	0	8.001	8.70E+04	0.45046	0.06109	0.180	0.024	7.374
		14.989	1.63E+05	1.75520	0.14362	0.199	0.016	12.221
	4	8.022	8.72E+04	0.46632	0.06597	0.185	0.026	7.069
		14.987	1.63E+05	1.69864	0.15906	0.193	0.018	10.679
	8	7.990	8.69E+04	0.45311	0.07025	0.181	0.028	6.450
		14.985	1.63E+05	1.64419	0.17754	0.187	0.020	9.261

Table 10: Values measured for the two yaw angles chosen.

Analysis	Velocity [m/s]	Re	Lift [N]	Drag [N]	C_L	C_D	C_L/C_D
No-Endplates	14.653	1.59E+05	3.896	2.389	0.463	0.284	1.631
	22.072	2.40E+05	9.368	4.710	0.491	0.247	1.989
	29.542	3.21E+05	7.603	4.874	0.222	0.142	1.560
	37.011	4.02E+05	12.848	6.105	0.239	0.114	2.105
Flat	14.653	1.59E+05	3.571	2.935	0.424	0.349	1.217
	22.072	2.40E+05	7.986	3.053	0.418	0.160	2.616
	29.542	3.21E+05	12.068	5.022	0.353	0.147	2.403
	37.011	4.02E+05	15.726	6.423	0.293	0.120	2.448
NACA2402	14.653	1.59E+05	3.204	3.676	0.381	0.437	0.872
	22.072	2.40E+05	7.282	2.590	0.381	0.136	2.811
	29.542	3.21E+05	14.764	4.831	0.432	0.141	3.056
	37.011	4.02E+05	17.126	6.217	0.319	0.116	2.755

Table 11: Values measured in the first run at the CAST tunnel.

fessor Luís Sousa for the time and effort put into printing all the parts needed to make the wind tunnel model; and André Oliveira and professor André Marta for the cooperation with the wind tunnel experiments at the Aerospace Laboratory.

References

[1] J. Katz. *Race Car Aerodynamics: Designing for Speed*. Bentley Publishers, 2003.

[2] Michael Trzesniowski. *Rennwagentechnik: Grundlagen, Konstruktion, Komponenten, Systeme*, chapter Aerodynamik Aerodynamics. Springer Fachmedien Wiesbaden, 2014.

[3] Formula Student Germany. Formula student rules 2020, 2020.

[4] F. R. Menter. Two-equation eddy-viscosity turbulence models for engineering applications. *AIAA Journal*, 1994.

[5] R. B. Langtry. *A Correlation-Based Transition Model using Local Variables for Unstructured Parallelized CFD codes*. PhD thesis, Universität Stuttgart, Fakultät Maschinenbau, 2006.

[6] C. J. Roy W. L. Oberkampf. *Verification and Validation in Scientific Computing*. Cambridge University Press, 2010.

[7] L. Eça M. Hoekstra. The numerical friction line. *Journal of Marine Science and Technology*, 2008.

[8] A. Pope J. B. Barlow, W. H. Rae. *Low-Speed Wind Tunnel Testing, 3rd Edition*. John Wiley and Sons, INC., 3rd edition, 1999.

[9] L. Traub. Experimental investigation of the effect of trip strips at low reynolds number. *Journal of Aircraft*, 2011.